J. Fluid Mech. (1980), *vol.* 100, *part* 1, *pp.* 1–29
Printed in Great Britain

Velocity distributions in plane turbulent channel flows

By M. M. M. EL TELBANY† AND A. J. REYNOLDS

Department of Mechanical Engineering, Brunel University, Uxbridge, Middlesex, England

(Received 16 August 1979)

Measurements of time-mean velocity have been made in a flat channel (aspect ratio 12 to 28), one of whose walls consists of a belt which can be moved in the direction of air blown through the channel or in the opposite direction. The wall layers generated in twenty-six turbulent flows, including plane Poiseuille and plane Couette cases, are compared with analytical results obtained by Kader & Yaglom and by Townsend. Empirical descriptions are developed for the viscous, logarithmic and gradient portions of these wall layers. The core regions of both Couette-type and Poiseuille-type flows are also described empirically. Parallels are drawn with developing boundary layers, and phenomena are identified that relate to the relaminarization of boundary layers.

1. Introduction

The measurements presented in this paper are intended to describe fully-developed turbulent flow between parallel walls, one of which may be in motion relative to the other. The velocity of the moving wall is in the direction of the mean flow through the channel (or directly opposed to it), and the hypothetical flow is therefore unidirectional. The flows actually studied are those in a flat channel (aspect ratio 12 to 28 in these tests) through which air is blown, and one of whose sides consists of a flat belt which can be moved either with the air blown through the channel or in the opposite direction. The experimental situation is shown schematically in figure 1. It is supposed that the motion near the mid-plane and exit from this channel, that is, in the vicinity of the access ports shown, approximates to the fully-developed unidirectional motion described above.

Earlier workers have studied two particular flows of the class considered here: pure pressure or plane Poiseuille flow (Laufer 1951; Comte-Bellot 1965; Hussain & Reynolds 1975) and pure shearing or plane Couette flow (Robertson & Johnson 1970; Huey & Williamson 1974; Szeri, Yates & Hai 1976). We know of no investigation of more varied combinations of blowing velocity and belt speed.

The empirical information to be presented has a number of immediate applications in engineering practice. Perhaps the most obvious is in predicting the motion within turbulent bearing films, which has been considered by Constantinescu (1959), Reynolds (1963), and Saibel & Macken (1974), amongst others. The usual approximation of lubrication theory represents bearing films by splicing together a series of fully-developed flows of the kind studied here. The results of this investigation relate also

† Permanent address: Faculty of Engineering, Helwan University, Egypt.

0022-1120/80/4501-1660 $02.00

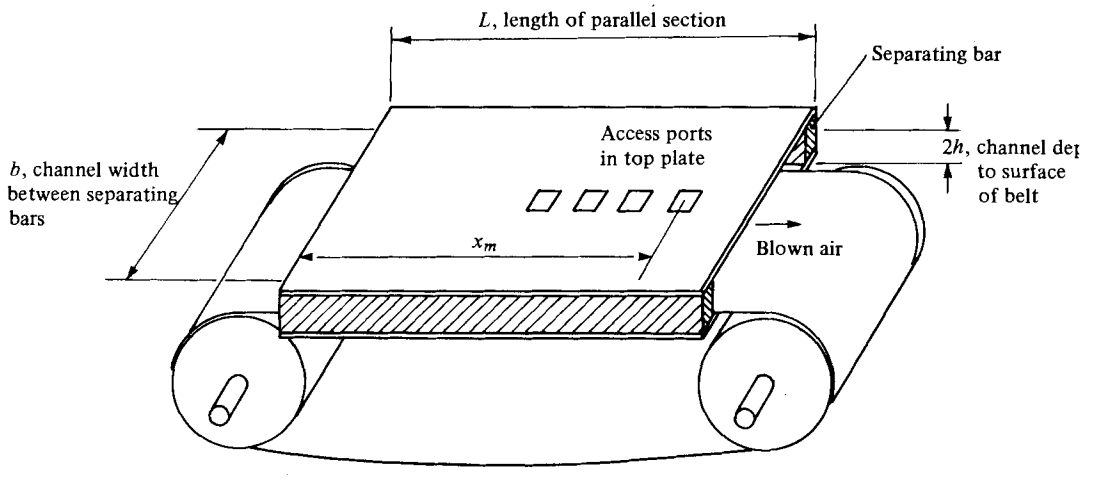

FIGURE 1. Schematic view of test channel showing the belt which provides the moving wall.

to the flow through a flat channel whose walls are of differing roughness (Hanjalić & Launder 1972) and, in a general way, to the flow through an annular passage.

The present measurements are of more general application in providing insight into the role of the shear-stress gradient in turbulent wall layers, in the absence of variability in the upstream 'history' of the flow. Thus the present study is complementary to that of Kader & Yaglom (1978) who collated results for many developing boundary layers exposed to adverse pressure gradients and deduced similarity laws that described many such flows with good accuracy. The present investigation is more restricted than the survey of Kader & Yaglom, in considering only wall layers that are nearly fully developed. However, its scope is wider in that we consider layers in which the shear stress decreases away from the wall, as well as those in which the shear stress exceeds that at the wall.

Kader & Yaglom adopted the streamwise gradient of kinematic pressure, $\rho^{-1}dP/dx$, as the parameter characterizing the departure of a boundary layer from the constant-stress pattern. This choice is inappropriate for fully-developed channel flow, where the cross-stream gradient of the stress may equal either the pressure gradient or its negative:

$$\frac{d\tau}{dy} = \left(\frac{d\tau}{dy}\right)_w = \pm \frac{dP}{dx} \tag{1.1}$$

throughout the flow. Since the local shear stress plays an important role in the energy balance and other dynamic aspects of the turbulence, we adopt the cross-stream stress gradient, $\rho^{-1}d\tau/dy$, as the relevant dynamic parameter, arguing that the pressure gradient is a relatively unimportant consequence of this stress gradient. Since the relationship (1.1) applies very near the wall in a developing boundary layer, it can be argued further that the relevance of the pressure gradient for the *inner* regions of a boundary layer arises from this connexion to the stress gradient at the wall. In other words, the success of Kader & Yaglom in correlating boundary-layer data using the gradient dP/dx may be primarily attributable to the fact that this parameter provides an estimate of the gradient $d\tau/dy$. Thus we conclude that the shear-stress gradient $(d\tau/dy)_w$ is the parameter that should be adopted in developing a unified view of the

wall layer, applicable to both channel flows and to boundary layers. Nevertheless, Kader & Yaglom's characterization of the boundary layer may provide a superior description of the whole of the layer, including a region beyond the wall layer proper.

Our experimental results will be fitted into two analytical schemes that have been proposed for wall layers with a strong cross-stream variation in shear stress: the equilibrium-layer model of Townsend (1961) and the similarity pattern of Kader & Yaglom (1978). The essential analytical results are set out in §2 below. The experimental results for channel flows are given in their basic form in §3 and are presented in the spirit of the two analytical schemes in §§4 and 5. In §6 we develop an overview of the class of flows under consideration, and consider briefly the way in which the core region can be defined.

To provide the basis for these developments, we take note of some fundamental relationships among the quantities measured and the parameters defining the experimental system. The time-mean velocity at a point in fully-developed flow of the kind under discussion will depend as follows on the parameters defining the motion:

$$U = f(y, \nu, h, \dot{v}, U_b), \tag{1.2}$$

where y is the distance measured from one wall, ν is the kinematic viscosity of the fluid, h is half the distance between the parallel walls, $\dot{v}$ is the flow rate per unit width of the channel, and U_b is the velocity of the moving belt. Here it has been assumed that both walls are effectively smooth, and the measurements show that this is the case for the experiments that have been conducted.

In order to bring together the results for various combinations of flow rate and wall velocity, we replace these parameters by the stresses τ_1 and τ_2 at the two walls:

$$U = f(y, \nu, h, \tau_1, \tau_2). \tag{1.3}$$

(Here and subsequently the subscript 1 denotes the wall at which the stress is the greater and the subscript 2 the other wall.) Even more convenient is the form

$$U = f(y, \nu, h, u_*, \alpha), \tag{1.4}$$

where $u_* = (\tau_w/\rho)^{\frac{1}{2}}$ is the friction velocity based on the shear stress at the wall from which y is measured, and α is the gradient of the kinematic shear stress.

The relationship of the parameters of equations (1.3) and (1.4) to the quantities $\dot{V}$ and U_b that are directly under the control of the experimenter cannot be obtained from simple arguments, but it is implicit in the experimental results to be presented below.

The parameters of equations (1.3) and (1.4) are connected by

$$|\alpha| = \frac{\tau_1 - \tau_2}{2\rho h} \quad \text{or} \quad \frac{2h|\alpha|}{u_{*1}^2} = 1 - \gamma. \tag{1.5}$$

Here $\gamma = \tau_2/\tau_1$ is the ratio of the shear stresses at the walls. For Couette flow

$$\gamma = 1 \quad \text{and} \quad h|\alpha|/u_{*1}^2 = 0,$$

while for Poiseuille flow

$$\gamma = -1 \quad \text{and} \quad h|\alpha|/u_{*1}^2 = 1.$$

Thus the ranges

$$1 \geqslant \gamma \geqslant -1 \quad \text{and} \quad 1 \geqslant h|\alpha|/u_{*1}^2 \geqslant 0$$

include all the flows under consideration.

Each of the flows studied contains two wall layers. We can distinguish between Couette-type flows which have

$$\gamma = \tau_2/\tau_1 > 0, \quad \alpha_1 = -|\alpha| < 0, \quad \alpha_2 = |\alpha| > 0,$$

and Poiseuille-type flows which have

$$\gamma = \tau_2/\tau_1 < 0, \quad \alpha_1 = \alpha_2 = -|\alpha| < 0.$$

Dimensional considerations allow us to write the result (1.4) in a variety of ways, of which

$$U/u_* = f(yu_*/\nu, \alpha h/u_*^2, y/h) \tag{1.6}$$

is as convenient as any. The near viscosity independence of the motion in the greater part of the flow is more easily taken into account by starting from the equivalent result

$$\frac{y}{u_*}\frac{dU}{dy} = f(yu_*/\nu, \alpha h/u_*^2, y/h). \tag{1.7}$$

The representation (1.4) may be compared with that adopted by Kader & Yaglom, namely

$$U = f(y, \nu, \delta, u_*, \rho^{-1}dP/dx). \tag{1.8}$$

Here the boundary-layer thickness δ has been adopted as the lateral length scale, and the streamwise gradient in kinematic pressure is taken as the second dynamic parameter, since the shear-stress gradient varies within a boundary layer. Following the arguments set out above, we may interpret this as

$$U = f(y, \nu, \delta, u_*, \rho^{-1}(d\tau/dy)_w) \tag{1.9}$$

thus establishing a more explicit link with the form adopted for channel flow.

2. Analytical models

2.1. *Viscous constant-stress layer*

If the influence of the stress gradient does not penetrate too close to the wall, there will exist near a smooth wall a region with

$$U/u_* = f(yu_*/\nu) \quad \text{only.} \tag{2.1}$$

Directly adjacent to the wall this reduces to

$$U/u_* = yu_*/\nu \quad \text{or} \quad U = (\tau_w/\mu)y \tag{2.2}$$

defining the linear sublayer, with $\mu = \rho\nu$ the dynamic viscosity. Although an analytical derivation of the velocity variation in the part of the viscous layer beyond the linear range (the so-called 'buffer layer') has not been developed, a number of sufficiently accurate semi-empirical formulae are available. Rannie's expression

$$U/u_* = 14{\cdot}5 \tanh (y_+/14{\cdot}5) \quad \text{for} \quad 0 < y_+ < 27{\cdot}5, \tag{2.3}$$

where $y_+ = yu_*/\nu$ is the scaled distance from the wall, is perhaps the easiest to manipulate. Others are mentioned in Reynolds (1974) and Hinze (1975).

2.2. *Viscosity-independent constant-stress layer*

For a region in which neither the stress gradient nor the distant wall (that is, the parameter h) influences the flow, and viscosity has ceased to have an effect, save through an effective slip at the wall, equation (1.7) reduces to

$$\frac{y}{u_*}\frac{dU}{dy} = A, \quad \text{a constant.}$$

Integration gives the familiar logarithmic formula

$$U/u_* = A\ln(yu_*/\nu) + B, \tag{2.4}$$

where B is a constant characterizing the change in velocity across the viscous layer.

The inner boundary of this region is that at which the viscous layer terminates; the limit to the applicability of equation (2.3) provides an estimate of this boundary.

2.3. *Gradient layer*

For a region somewhat further from the wall, it may happen that the stress gradient is dominant, while the wall stress and distant wall have little influence, and viscosity is significant only through the 'slip' near the wall. Since none of the parameters ν, h and u_* plays a part, equation (1.7) can be written

$$\frac{y}{u_*}\frac{dU}{dy} = f(\alpha y/u_*^2) \propto (\alpha y/u_*^2)^{\frac{1}{2}},$$

or

$$\left(\frac{y}{\alpha}\right)^{\frac{1}{2}}\frac{dU}{dy} = \tfrac{1}{2}K_1, \quad \text{a constant.}$$

Integration gives the half-power law

$$U/u_* = K_1(\alpha y/u_*^2)^{\frac{1}{2}} + K_2, \tag{2.5}$$

where K_1 and K_2 are constants analogous to those of the logarithmic law (2.4).

Kader & Yaglom have related these constants and have estimated the inner limit of this region by matching the velocity and its gradient to those of the layer closer to the wall. If there is a logarithmic layer between the gradient layer and the wall, these conditions give

$$Y_+ = (2A/K_1)^2 u_*^3/\alpha\nu \quad \text{and} \quad K_2 = A\ln y_+ + B - 2A. \tag{2.6a}$$

If there is no logarithmic layer, matching with the linear layer gives

$$Y_+ = (K_1/2)^2(\alpha\nu/u_*^3) = -K_2. \tag{2.7a}$$

Introducing the parameter

$$\Gamma = 4A^2(u_*^3/\alpha\nu)/K_1^2,$$

we can write these results as

$$Y_+ = \Gamma \quad \text{and} \quad K_2 = A\ln\Gamma + B - 2A, \tag{2.6b}$$

$$Y_+ = -K_2 = A^2/\Gamma. \tag{2.7b}$$

These simple calculations serve to suggest that the relationship between the constants K_1 and K_2 will depend upon the single parameter Γ. Obviously it is impossible for both K_1 and K_2 to be absolute constants, that is, for both to be independent of a

parameter such as $u_*^3/\alpha\nu$. The estimates obtained above for the value of y_+ at which the gradient layer meets an inner layer turn out to be low by a considerable factor, but we shall find that the predictions of $K_2 = f(\Gamma)$ are reasonably accurate. This can be so because the curves being matched are nearly coincident over a considerable range of y_+; hence matching can be imposed at rather different values of y_+ without significantly altering the prediction of the 'slip constant' K_2.

2.4. *Generalized gradient layer*

Although boundary-layer velocity profiles commonly contain considerable portions where $U \propto y^{\frac{1}{2}}$, as predicted in equation (2.5), it has been found that the constants K_1 and K_2 vary markedly from layer to layer, that is, as the role of the gradient α varies. Since the dependence on the co-ordinate y has been correctly accounted for, and viscosity influences only the constant K_2, the appropriate limiting form of equation (1.7) must be

$$\frac{y}{u_*}\frac{dU}{dy} = f(\alpha y/u_*^2, \alpha h/u_*^2) = (\alpha y/u_*^2)^{\frac{1}{2}} f(\alpha h/u_*^2).$$

Thus we see that

$$K_1 = f(\alpha h/u_*^2). \tag{2.8}$$

From equation (1.6) we see now that the constant K_2 may have the form

$$K_2 = f(\alpha h/u_*^2, \alpha\nu/u_*^3).$$

However, the results (2.6, 7) suggest that the two parameters occur only in the combination Γ, so that

$$K_2 = f(\Gamma) = f(u_*^3/\alpha\nu K_1^2), \tag{2.9}$$

with dependence on the parameter $\alpha h/u_*^2$ introduced through K_1.

2.5. *Linear-stress layer*

The analysis of §2.3 makes sense only if the stress distribution

$$\tau = \tau_w + \rho\alpha y \tag{2.10}$$

is closely approximated by $\tau = \rho\alpha y$ through much of the wall layer. This may be so for a wall layer within which the stress increases away from the wall ($\alpha > 0$), but is unlikely to be the case if the stress falls ($\alpha < 0$) and the wall stress influences the local stress at least over the range

$$y < -\tau_w/\rho\alpha = -u_*^2/\alpha.$$

It is possible, however, that a gradient layer may exist in a region beyond the plane on which $\tau = 0$, that is, for

$$y > -u_*^2/\alpha \quad \text{with} \quad -\alpha h/u_*^2 \gg 1.$$

Townsend (1961) has deduced a velocity distribution corresponding to the stress variation (2.10) by assuming a form of equilibrium in which the lateral diffusion of turbulence energy is characterized by a constant B_1, the diffusion term of the energy equation having been scaled with the local shear stress. Thus, setting $\lambda = \alpha h/u_*^2$ for compactness, we find

$$\frac{\Delta U}{u_*} = \frac{U}{u_*} - A \ln\left[\frac{4u_*^3}{\alpha\nu}\frac{(1+\lambda y/h)^{\frac{1}{2}}-1}{(1+\lambda y/h)^{\frac{1}{2}}+1}\right] = (2A+3B_1)(1+\lambda y/h)^{\frac{1}{2}} + C. \tag{2.11}$$

The constant $4u_*^3/\alpha\nu$ is introduced to ensure that

$$\Delta U/u_* \to U/u_* - A\ln y_+ \to 2A + 3B_1 + C \quad \text{as} \quad \lambda \to 0$$

to give a constant-stress layer. Comparison with equation (2.4) indicates that

$$2A + 3B_1 + C = B \tag{2.12}$$

in this limit.

At the other limit, $\lambda y/h \gg 1$, we note that equation (2.11) gives

$$U/u_* = A\ln(4u_*^3/\alpha\nu) + (2A + 3B_1)(\alpha y/u_*^2)^{\frac{1}{2}} + C.$$

Thus we see that Townsend's model incorporates both logarithmic and gradient layers in a comprehensive wall-layer model whose applicability is not obviously limited to $\lambda > 0$. Comparison with equation (2.5) indicates that

$$\left.\begin{aligned} A\ln(4u_*^3/\alpha\nu) + C &= K_2, \\ 2A + 3B_1 &= K_1. \end{aligned}\right\} \tag{2.13}$$

Since A is known to be essentially a universal constant, equation (2.8) demonstrates that $B_1 = f(\alpha h/u_*^2)$ is not. Which of the two constants C and K_2 varies least with the parameters Γ or $u_*^3/\alpha\nu$ we shall discover from the experimental results.

2.6. *Core regions*

For the middle part of both Couette and Poiseuille flows the eddy viscosity is more-or-less constant, and a simple analysis (see, for example, Reynolds 1974) gives the velocity defect distributions

$$(U_c - U)/u_* = R_f(1 - y/h) \quad \text{for Couette flow,} \tag{2.14}$$

$$= \tfrac{1}{2}R_f(1 - y/h)^2 \quad \text{for Poiseuille flow,} \tag{2.15}$$

where U_c is the velocity in the mid-plane, and $R_f = u_*h/\epsilon_c$ is a flow constant, or turbulence Reynolds number, which incorporates the constant eddy viscosity ϵ_c.

The eddy diffusivity is far from uniform in the 'core' regions of the channel flows to be discussed here, but the expressions (2.14, 15) may still provide convenient descriptions of the relatively small velocity variation in the central part of the channel. Another possible approach is the introduction of the more general form

$$(U_c - U)/u_* \propto |1 - y/h|^n. \tag{2.16}$$

For plane Poiseuille flow, $n \simeq 1{\cdot}9$.

A problem which we shall meet when discussing the central region of general channel flow is that of deciding how the effective friction velocity for that region should be defined.

3. Experimental results

3.1. *Apparatus*

The parallel section of the channel shown in figure 1 is 2440 mm long; the main measurements were made at the centre of the channel at a station $x_m = 1980$ mm from the blowing end. The belt forming the moving floor is 1200 mm wide, some 20 mm less than the channel breadth measured between the separating bars which form the vertical sides. To eliminate possible flapping, the belt is supported from underneath

by an aluminium-surfaced plate. Appropriate tensioning and central running on the slightly crowned rollers are achieved by screw adjustment of the bearings supporting one of the rollers.

The plate forming the top of the channel is stiffened to maintain uniformity of channel depth and is clamped to the separating bars, which can be changed to vary the depth. The depths used in these experiments range from $2h = 44$ to 101 mm, giving aspect ratios $b/2h = 28$ to 12, and scaled development distances $x_m/2h = 45$ to 20. The flow into the test channel is supplied by a specially constructed wind tunnel, consisting of centrifugal fan, diffuser, filters and contraction. To expedite the development of the flow, turbulent activity is introduced before the air enters the parallel-sided duct, by a coarse mesh of expanded metal located some 150 mm upstream of the parallel section. Hence the development distances quoted above give a somewhat conservative idea of the degree of development of the flow. The mean-velocity and shear-stress measurements presented below do not provide critical tests of flow development, but measurements of turbulence intensities (to be presented elsewhere) demonstrate that the turbulent motion is substantially fully developed at the mean measuring station, $x_m = 1980$ mm.

Mean-velocity profiles were measured using a DISA normal hot-wire probe (type 55P11) in conjunction with a DISA 55M system constant-temperature anemometer, a 55M25 linearizer and a Datron 1045 digital voltmeter. The turbulent shear stress was measured with a DISA X-wire probe (type 55P61) in conjunction with two such channels, a 55D35 r.m.s. voltmeter and the digital voltmeter.

The probes were calibrated in pure pressure flow through the test channel itself, and the results from the X-wire were checked by comparisons with wall stresses determined from (i) the wall-pressure drop along the channel, and (ii) the linear velocity variation near the wall.

The position of the hot-wire probes within the channel could be controlled within 0·01 mm by a micrometer traversing mechanism. The belt speed was determined by a counter activated by magnetic strips on the belt.

3.2. *Basic results*

Table 1 details the tests carried out. The first group (cases 1–9) are the Couette-type flows ($\gamma > 0$) to be considered in detail; the second group (cases 10–15) are the Poiseuille-type flows ($\gamma < 0$) to be looked at in detail. For the remaining flows (cases 16–26) the same measurements were made, but for the most part they reproduce the features illustrated by the cases above and will not be described so completely.

All but four of these flows were generated by running the belt in the same direction as the blown flow of air. For the cases of counter-motion (12, 13, 14, 22) the region of reversed flow moving into the channel with the belt was very thin, extending at most to $y/2h = 0{\cdot}05$. Hence a close approximation to full development can still be achieved at $x_m = 1980$ mm, despite the small amount of air drawn into the channel from the nominal exhaust section at $x = 2440$ mm.

Figure 2 shows the shear-stress variations in the fifteen flows selected for study; their linearity gives some evidence of the degree of development of the flows. The wall stresses were found by extrapolating these straight lines to the walls. Here, and in other measurements, it is possible to move the probe close to the fixed wall, but not as

	Overall characteristics						Parameters for high-stress wall			Parameters for low-stress wall				
Case	$2h$ (mm)	U_b (ms^{-1})	U_m (ms^{-1})	U_a (ms^{-1})	$\frac{Re_a}{1000}$	$\frac{Re_b}{1000}$	u_{*1} (ms^{-1})	α_1	λ_1	u_{*2} (ms^{-1})	α_2	λ_2	γ	Wall in motion
1	66	12·84	12·84	6·42	28·50	57·01	0·282	0	0	0·282	0	0	1·000	2
2	66	12·84	12·84	7·28	32·33	57·01	0·328	−0·808	0·248	0·233	0·808	0·491	0·504	2
3	66	12·84	12·84	8·06	35·80	57·01	0·362	−1·486	−0·375	0·1809	1·486	1·499	0·250	2
4	66	12·84	12·84	8·14	36·14	57·01	0·357	−1·510	−0·391	0·1667	1·510	1·795	0·217	1
5	66	12·84	12·84	8·81	39·11	57·01	0·383	−1·960	−0·442	0·1305	1·960	3·809	0·116	1
6	66	8·59	8·59	6·71	29·79	38·14	0·313	−1·430	−0·481	0·0615	1·430	12·45	0·0386	1
7	101	17·08	17·08	14·55	98·80	116·05	0·600	−3·548	−0·497	0·0400	3·548	112·0	0·0044	1
8	101	12·84	12·84	11·38	77·30	87·24	0·485	−2·323	−0·498	0·0229	2·323	223·7	0·00223	1
9	101	8·59	8·59	7·79	52·94	58·36	0·350	−1·212	−0·499	0·0084	1·212	867·4	0·00057	1
10	66	12·84	13·25	12·40	55·07	57·01	0·564	−4·830	−0·5014	0·0300	−4·83	−177·2	−0·0028	2
11	66	12·84	16·33	15·10	67·05	57·01	0·679	−7·500	−0·537	0·1860	−7·50	−7·16	−0·075	2
12	66	12·84	21·57	20·11	89·28	57·01	0·880	−14·30	−0·611	0·4142	−14·3	−2·76	−0·2215	1
13	66	12·84	24·01	22·40	99·48	57·01	0·978	−18·50	−0·640	0·518	−18·5	−2·28	−0·2805	1
14	66	8·59	23·62	21·90	97·25	38·14	0·961	−20·80	−0·742	0·670	−20·8	−1·529	−0·485	1
15	66	—	16·00	14·55	64·60	—	0·659	−13·14	−1·000	0·659	−13·1	−1·000	−1·000	—
16	44	12·84	12·84	6·42	19·00	38·00	0·293	0	0	0·293	0	0	1·000	2
17	44	17·08	17·08	8·54	25·28	50·56	0·378	0	0	0·378	0	0	1·000	2
18	66	17·08	17·08	8·54	37·92	75·83	0·363	0	0	0·363	0	0	1·000	2
19	66	12·84	12·84	6·12	27·17	57·01	0·303	−0·314	−0·113	0·267	0·314	0·145	0·775	2
20	66	12·84	12·84	3·31	14·70	57·01	0·431	−2·640	−0·468	0·1089	2·64	7·38	0·0635	2
21	66	12·84	12·84	3·17	14·07	57·01	0·435	−2·70	−0·471	0·1035	2·70	8·33	0·0566	1
22	66	12·84	18·27	16·89	75·02	57·01	0·740	−9·40	−0·566	0·269	−9·40	−4·28	−0·132	1
23	66	8·59	13·81	12·87	57·13	38·14	0·600	−6·43	−0·591	0·256	−6·43	−3·25	−0·1816	2
24	66	8·59	15·05	14·02	62·24	38·14	0·645	−7·722	−0·613	0·306	−7·72	−2·72	−0·225	2
25	44	—	25·80	23·52	69·62	—	1·040	−49·16	−1·000	1·040	−49·2	−1·000	−1·000	—
26	66	—	12·60	11·42	50·70	—	0·514	−8·00	−1·000	0·514	−8·00	−1·000	−1·000	—

TABLE 1. Details of tests.

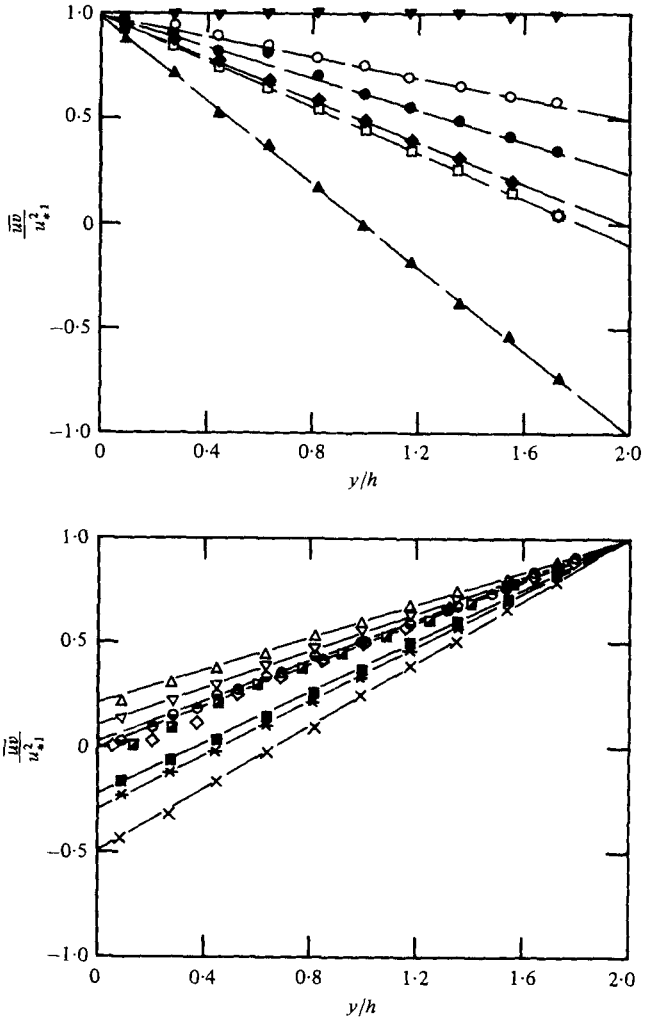

FIGURE 2. Distributions of kinematic shear stress at measuring station (y measured from fixed wall). ▼, 1; ○, 2; ●, 3; △, 4; ▽, 5; ◒, 6; ◓, 7; ◪, 8; ◇, 9; ◆, 10; □, 11; ■, 12; *, 13; ×, 14; ▲, 15.

near to the moving wall, since any local protuberance on the belt may damage the instrument. In consequence, one of the two wall layers within each flow can be examined in more detail than can the other.

Figure 3(*a*) gives the velocity profiles for the nine Couette-type flows and figure 3(*b*) those for the six Poiseuille-type flows that have been selected for the particular study. If y is measured from the fixed wall U is the local fluid velocity; if y is measured from the moving wall U is the relative velocity of the fluid. The maximum velocities U_m given in table 1 were obtained from these figures, and the average velocities U_a are derived by integrating these profiles. Note that the Reynolds numbers Re_a and Re_b are generally above 10^4 and in some cases close to 10^5. These are rather higher Reynolds numbers than those achieved in other moving-wall experiments, which are typically in the range 5×10^3 to 3×10^4.

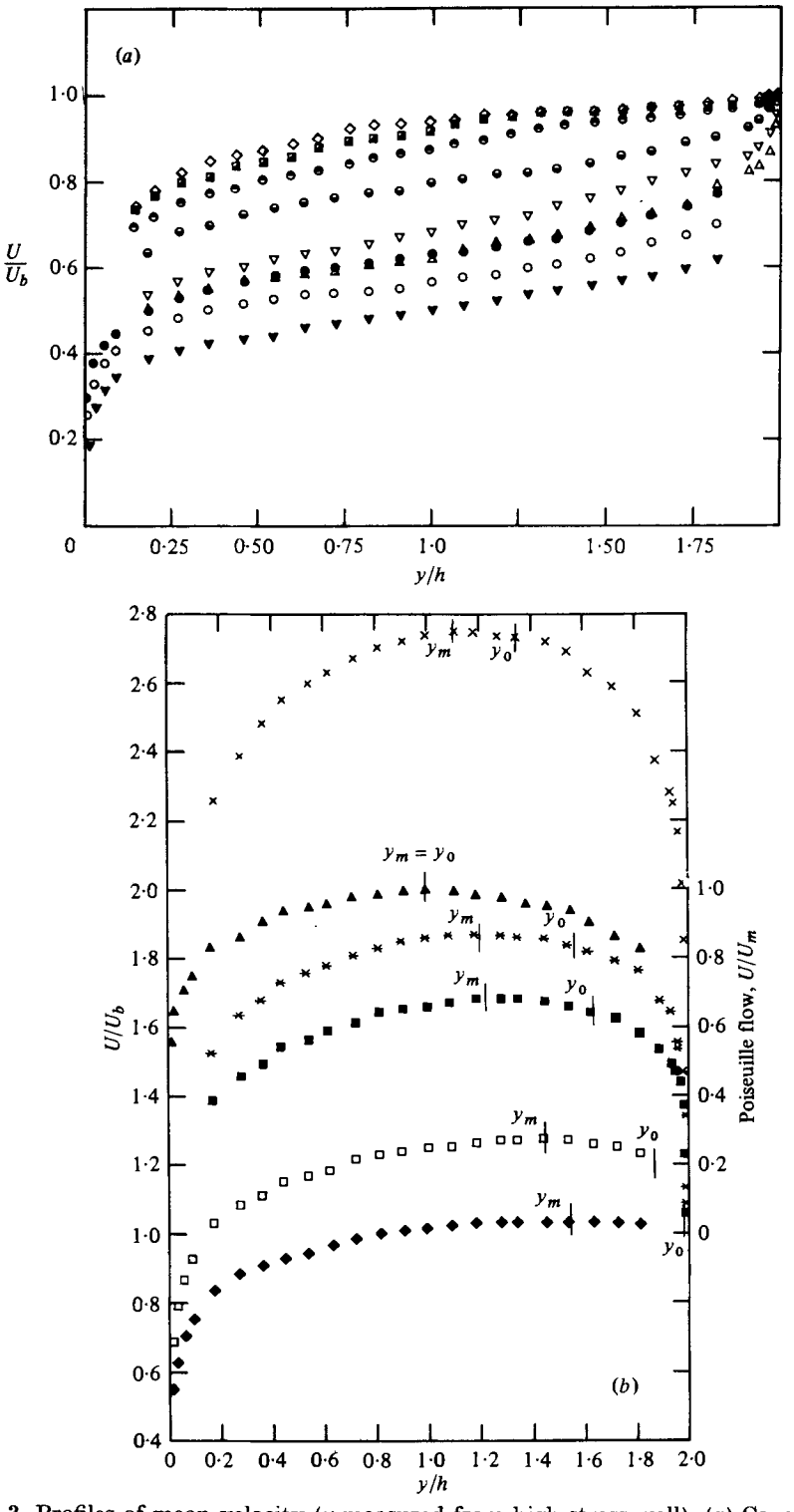

FIGURE 3. Profiles of mean velocity (y measured from high-stress wall). (a) Couette-type flows ($1 \geqslant \gamma > 0$). (b) Poiseuille-type flows ($0 > \gamma \geqslant -1$); points of maximum velocity (y_m) and shear stress (y_0) are indicated. For the symbols see figure 2.

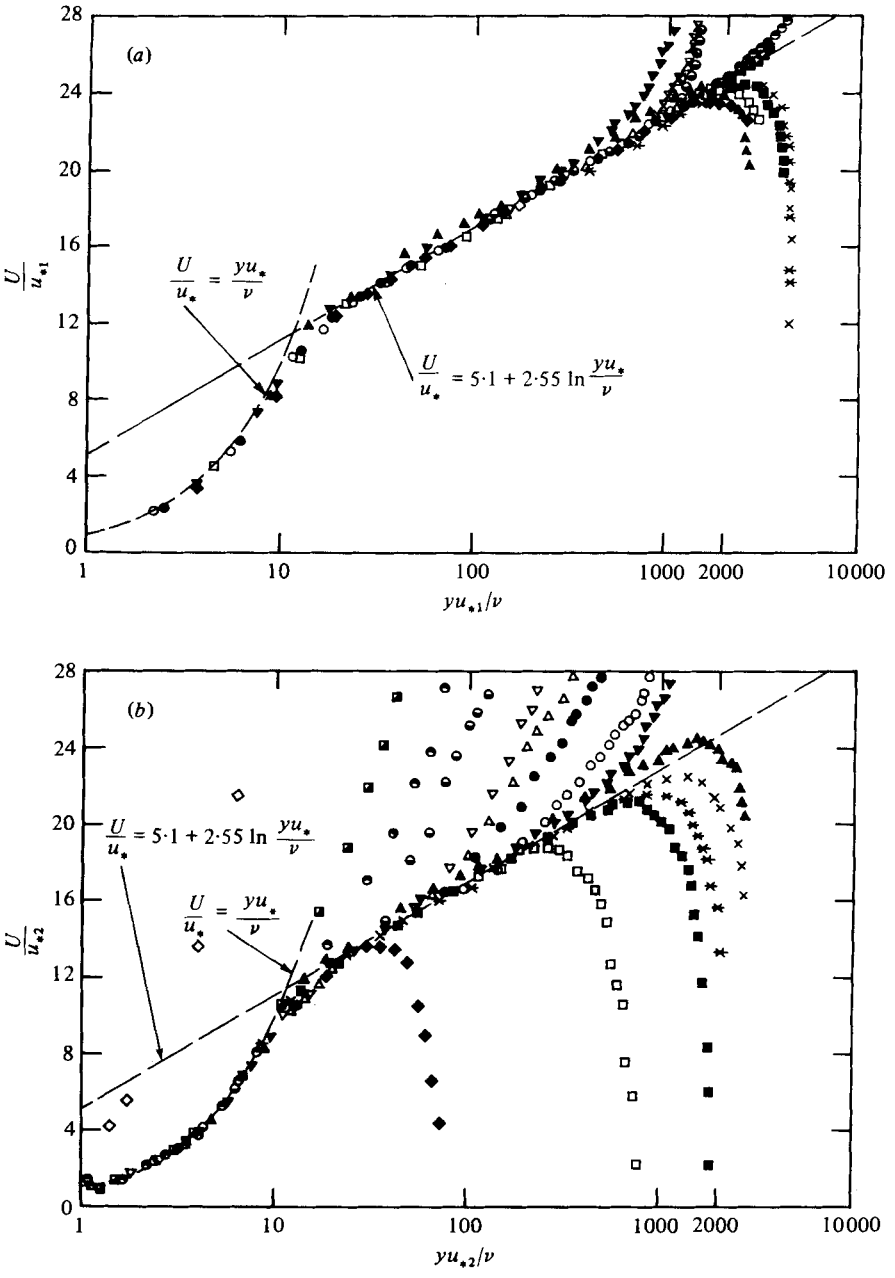

FIGURE 4. Semi-logarithmic plotting of velocity profiles. (*a*) y measured from the high-stress wall. (*b*) y measured from the low-stress wall. For the symbols see figure 2.

4. Reduction of data using the scheme of Kader & Yaglom

4.1. *Viscous layer*

Figure 4 shows the velocity distributions adjacent to the walls, plotted according to the constant-stress scaling of equation (2.1). A noteworthy feature of the measurements in the viscous layers is the abruptness of the transition to the logarithmic law. In these measurements the buffer layer is confined to the range $7 < y_+ < 22$, having only about two-thirds the thickness commonly quoted.

None of the semi-empirical descriptions of the viscous layer reproduces this behaviour (in particular, they indicate a significant departure from the linear law for $y_+ < 7$), but equation (2.3) is closer than most such formulae to the buffer-layer velocity variation found here.

4.2. *Logarithmic layer*

Figure 4(*a*) shows velocity distributions adjacent to the wall with the larger absolute stress. All of these results are represented within $1\frac{1}{2}\%$ by a single logarithmic formula

$$U/u_* = A \ln y_+ + B \tag{4.1}$$

over the range $20 < y_+ < 400$, with $A = 2{\cdot}55 \pm 0{\cdot}1$ and $B = 5{\cdot}1 \pm 0{\cdot}15$. Departures from this trend are in part attributable to experimental scatter, but it is possible to distinguish some dependence on flow type, with $B = 5{\cdot}25$ for Poiseuille flow, and $B = 5{\cdot}0 \pm 0{\cdot}10$ for most of the other layers. The logarithmic law remains valid for higher values of y_+ in those cases in which the stress falls off significantly away from the wall; seemingly there is a cancelling of the opposing effects of smaller stresses and of penetration of the outer or core flow. Figure 4(*b*) gives the velocity distribution near the low-stress wall. As would be expected, the logarithmic layer is eroded, and ultimately vanishes, as the stress gradient increases in importance. Even so, the logarithmic layers that remain are accurately prescribed by the constants A and B given above.

4.3. *Gradient layer*

In figure 5 velocity variations near the low-stress wall are plotted against $(\alpha y)^{\frac{1}{2}}$ in order to investigate the validity of the hypotheses underlying the gradient law (2.5). In selecting lines to represent the half-power law and so to determine the constants K_1 and K_2, it is important to take note of the inner limit to the applicability of this law. While it may be possible to describe a larger part of the velocity profile with the form $U = ay^{\frac{1}{2}} + b$ (and this procedure may prove useful in simple calculation schemes), identification of the gradient layer proper requires that we set aside points which we know, from figure 4(*b*), to lie within the region of logarithmic velocity variation.

Figure 6 presents the constants of the generalized gradient law as functions of the parameters of equations (2.8, 9). In figure 6(*a*) are shown also:

(i) an empirical formula

$$K_1 = 19\lambda^{-\frac{1}{3}}, \tag{4.2}$$

which represents the present measurements over the range $1 < \lambda < 400$;

(ii) an empirical formula

$$K_1 = (200/\lambda + 20)^{\frac{1}{2}} \quad \text{with} \quad \lambda = \delta\alpha/u_*^2 \tag{4.3}$$

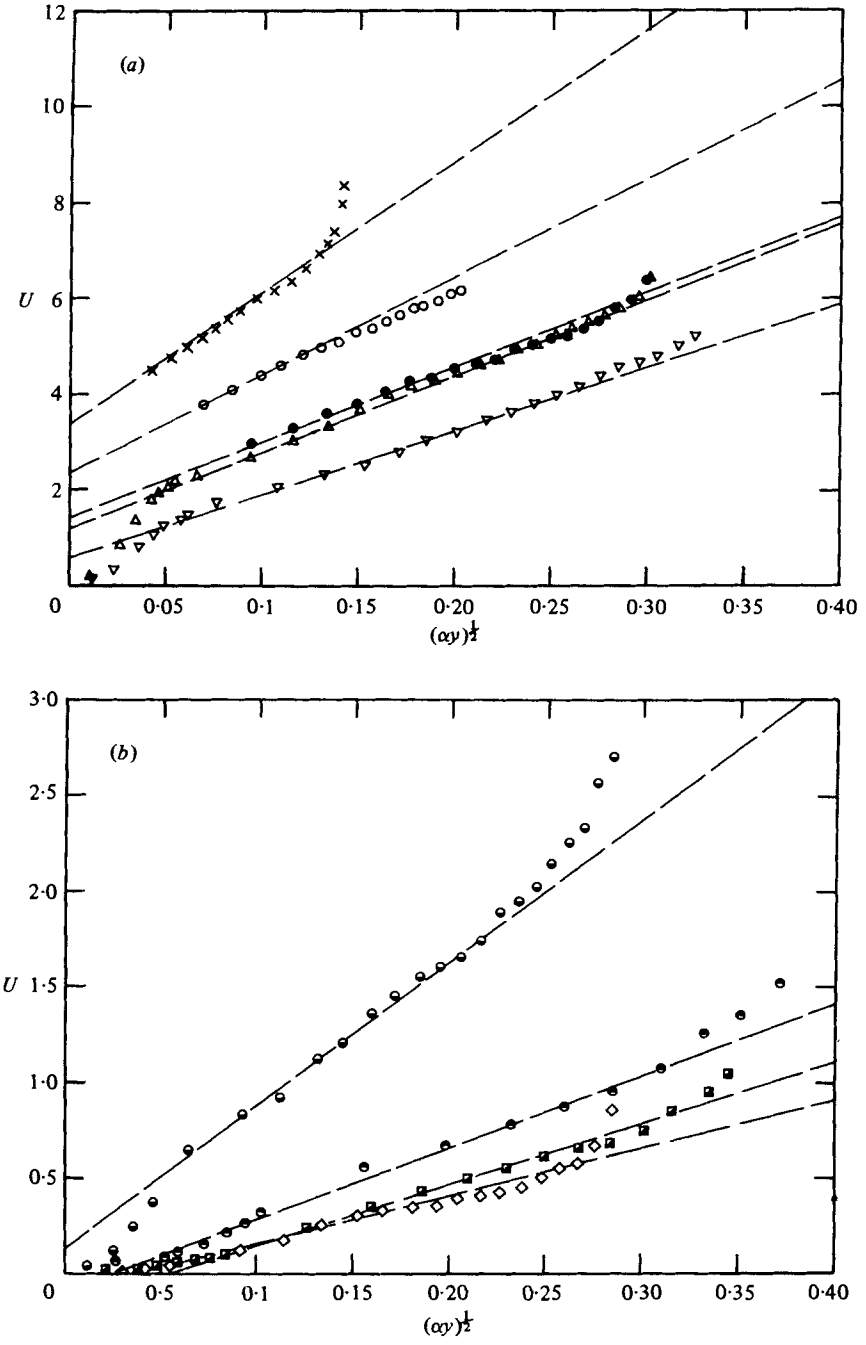

FIGURE 5. Plots to determine the gradient layer: positive stress gradient α (y measured from the low-stress wall). (*a*) Cases with moderate wall stress. (*b*) Cases with small wall stress. ○, 2; ●, 3; △, 4; ▽, 5; ◒, 6; ◓, 7; ◪, 8; ◇, 9; ×, 19.

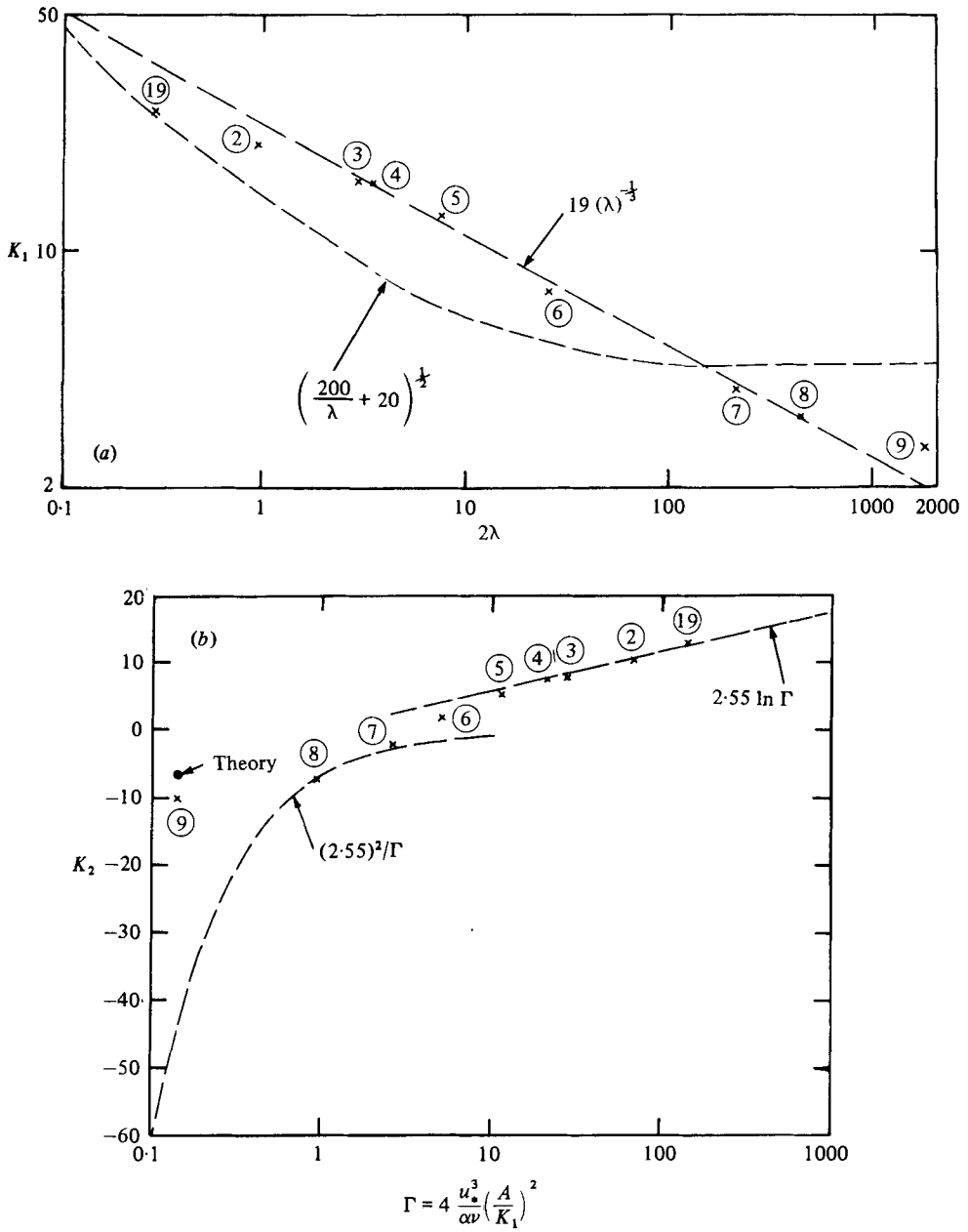

FIGURE 6. Constants for Kader & Yaglom's description of the gradient layer (equations (2.5), (2.8), (2.9)). (*a*) Gradient layer constant K_1. The power law (defined here by a straight line) describes the present measurements over a wide range. The other curve is Kader & Yaglom's empirical formula for this constant, as determined from profiles measured in developing boundary layers. (*b*) Slip constant K_2. The curves (equations (2.6*b*), (2.7*b*)) are obtained by matching gradient and constant-stress layers. The calculated point on the left is obtained using the analysis of the appendix.

found by Kader & Yaglom to represent the half-power regions within developing boundary layers.

Comparison of the boundary-layer and channel-flow results is made difficult by the differing length scales that have to be adopted for the two kinds of flow. However, it is possible to compare the asymptotic values of K_1 for $\lambda \gg 1$. The channel-flow measurements suggest a rather lower value, $K_1 \simeq 3$, compared to Kader & Yaglom's $K_1 \simeq 4{\cdot}5$. In addition to values measured from figure 5, figure 6(*b*) shows the predictions of K_2 obtained by introducing the measured values of K_1 into equations (2.6*b*), (2.7*b*). The generally good agreement with the predictions based on the assumption of a sharp transition between constant-stress layer and gradient layer is consistent with the rather abrupt transitions evident in figure 4(*b*).

The value of K_2 for the smallest value of Γ is not in accord with the prediction based on matching with a constant-stress viscous layer. In this extreme case, with a value of Γ somewhat smaller than those encountered by Kader & Yaglom, the assumption of a linear velocity variation is unrealistic. The appendix contains an analysis based on a parabolic velocity distribution in the viscous region (that is, for $\tau = \rho\alpha y$). For this model

$$K_2 = f(\Gamma, \alpha h/u_*^2).$$

The prediction of this theory for the particular case of interest here is marked in figure 6(*b*).

5. Comparison with Townsend's linear-stress model

The plots of $\Delta U/u_*$ versus $(1+\lambda y/h)^{\frac{1}{2}}$ in figures 7, 9 and 10 are designed to pick out the half-power element of the velocity variation, if one exists.

Figure 7 presents data for Couette-type flows where α, $\lambda > 0$. As would be anticipated, there exist considerable regions in which the residual element of the velocity variation can be described by

$$\Delta U/u_* = (2A + 3B_1)\,(1+\lambda y/h)^{\frac{1}{2}} + C.$$

The values of the constant $2A + 3B_1$ found from these plots are given in figure 8(*a*). Since the data has been analysed in a different way, these values differ somewhat from the rather similar constant K_1 given in figure 6(*a*). Nevertheless, equation (4.2) still provides a reasonable prediction over a wide range of the parameter λ. The diffusion constant B_1, far from being independent of flow type, varies from $B_1 \simeq -0{\cdot}7$ for $\lambda > 100$ to $B_1 \simeq 5$ for $\lambda < 1$. Marked variations in the apparent value of B_1 were pointed out by Reynolds (1965).

The range of the constant C evident in figure 8(*b*) is about the same as that of the alternative constant K_2. (Here the parameter Γ has been obtained by replacing K_1 by $2A + 3B_1$.) In this respect there is little to choose between Townsend's and Kader & Yaglom's representations of the velocity distributions.

Turning in figure 9 to Poiseuille-type flows where α, $\lambda < 0$, we can again discern significant regions of half-power variation. Note that the range of $(1+\lambda y/h)^{\frac{1}{2}}$ is in this case bounded by the zero-stress plane. The plane of maximum velocity lies within the range considered; indeed, we shall see later that it is near this plane that the validity of the half-power laws terminates.

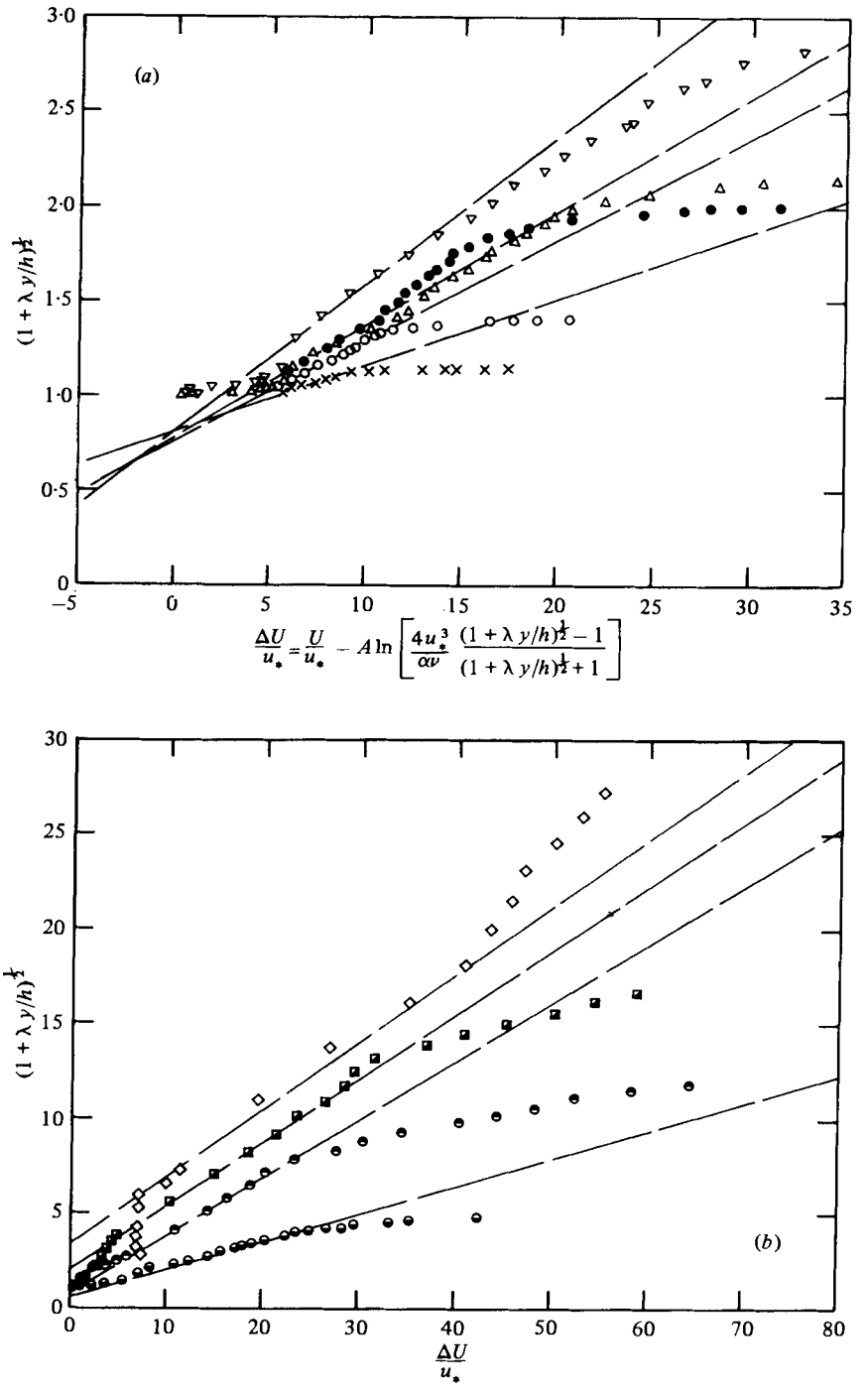

FIGURE 7. Plots to determine the residual velocity variation (equation (2.11)) of Townsend's description of the wall layer: positive stress gradient α (y measured from the low-stress wall). (*a*) Cases with moderate wall stress. (*b*) Cases with small wall stress. See figure 5 for the symbols.

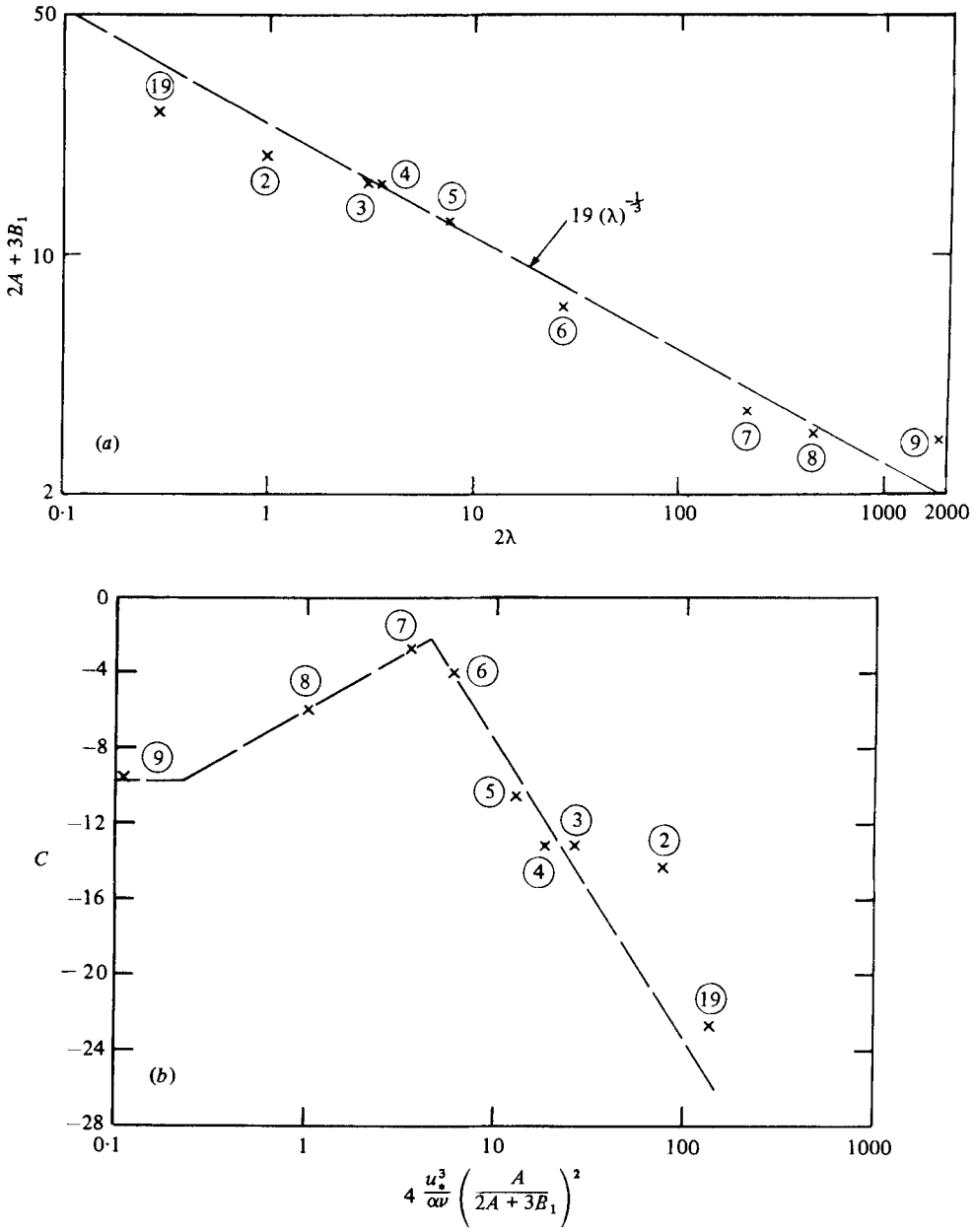

FIGURE 8. Constants for Townsend's description of the gradient layer: positive stress gradient α. (*a*) Gradient constant $2A + 3B_1$. The power law is that of figure 6(*a*). (*b*) Slip constant C.

We consider next the constants defining the linear regions in figure 9. The value of the slope $2A + 3B_1$ is close to 4 for all of the gradient layers that can be distinguished (all the high-stress walls, Poiseuille flow and low-stress wall for case 14). The corresponding diffusion constant is $B_1 \simeq -0{\cdot}3$. For most of the profiles the constant C is close to 1·7, but for Poiseuille flow $C \simeq 2{\cdot}7$.

Although there are discernible linear regions in other profiles of figure 9(*b*) – with

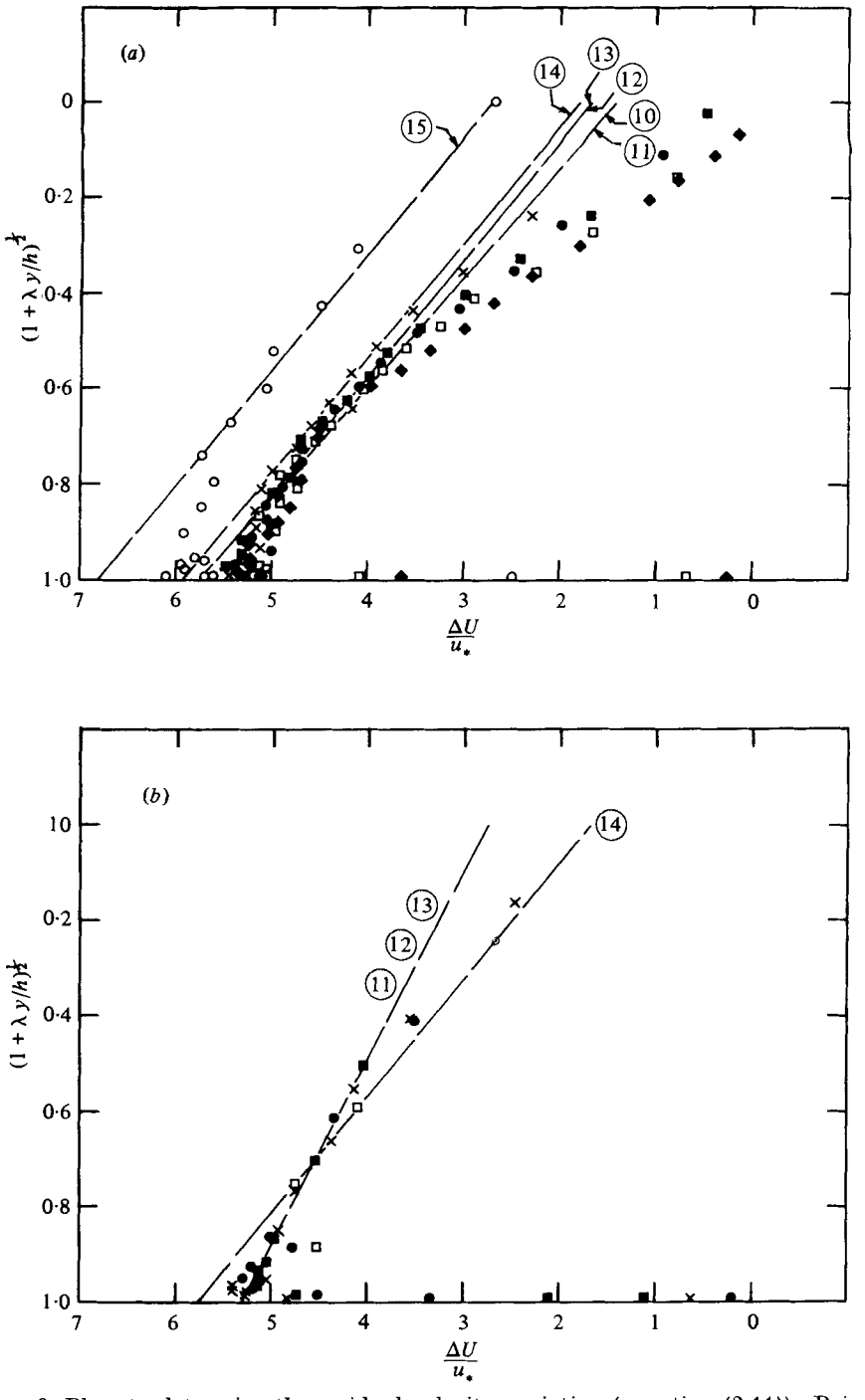

FIGURE 9. Plots to determine the residual velocity variation (equation (2.11)): Poiseuille-type flows; negative stress gradient α. (*a*) y measured from the high-stress wall. (*b*) y measured from the low-stress wall. ◆, 10; □, 11; ■, 12; ●, 13; ×, 14; ○, 15.

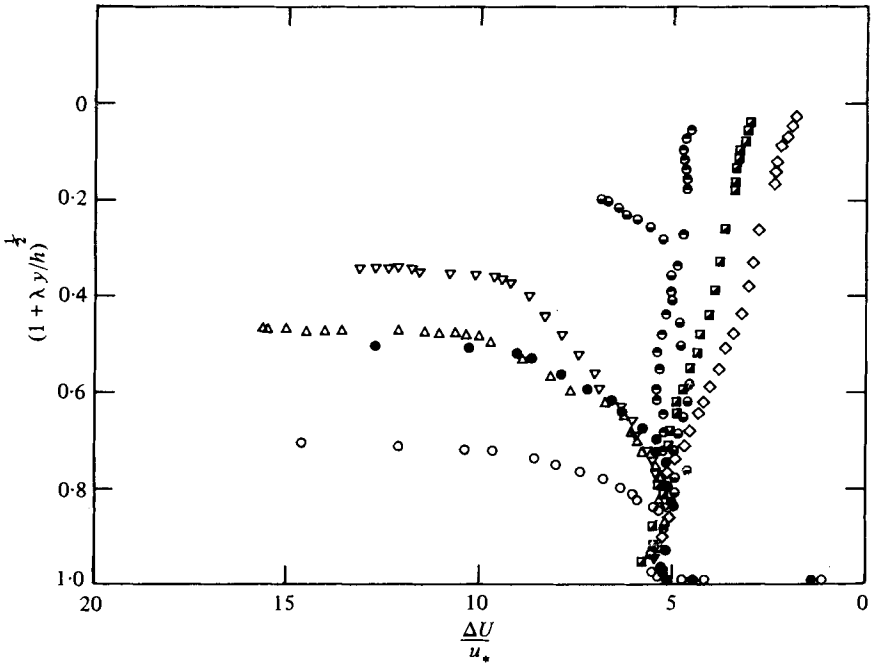

FIGURE 10. Residual velocity variation for Couette-type flows: high-stress side. See figure 2 for the symbols.

a slope near 2 – these regions are in fact quite well described by the logarithmic formula, and there is little justification for introducing a gradient layer.

No very obvious relationship exists between the constants pertaining for $\alpha, \lambda > 0$ and for $\alpha, \lambda < 0$, save that the slope $2A + 3B_1$ for $\lambda < 0$ is close to the asymptotic value for $\lambda \gg 0$.

The flows considered in figure 9 are those with a relatively large stress gradient ($-\lambda > 0{\cdot}5$), in which it is possible that a gradient layer may develop between the logarithmic layer and the region much influenced by the distant wall. In the flows to which figure 10 relates, for which $-\lambda < 0{\cdot}5$, this does not occur; it appears that there is a direct transition from a logarithmic layer to a flow much influenced by the activity at the other wall. These are the Couette-type flows considered earlier in figures 7 and 8, but we now examine the high-stress wall; the other wall lies within the range $0 < (1+\lambda y/h)^{\frac{1}{2}} < 1$. Although half-power laws do not provide a useful representation of these flows, the simple statement $\Delta U/u_* \simeq 5{\cdot}1$ represents a major part of the velocity variation.

6. An overview of the channel flows

6.1. *Boundaries between regions*

We now gather together what we have learned about the validity of the similarity laws proposed in §2, in order to develop a comprehensive view of the class of motions under discussion. Figure 11 shows the apparent boundaries between constant-stress and gradient layers (taken from figures 4 and 9) and between gradient layers and core

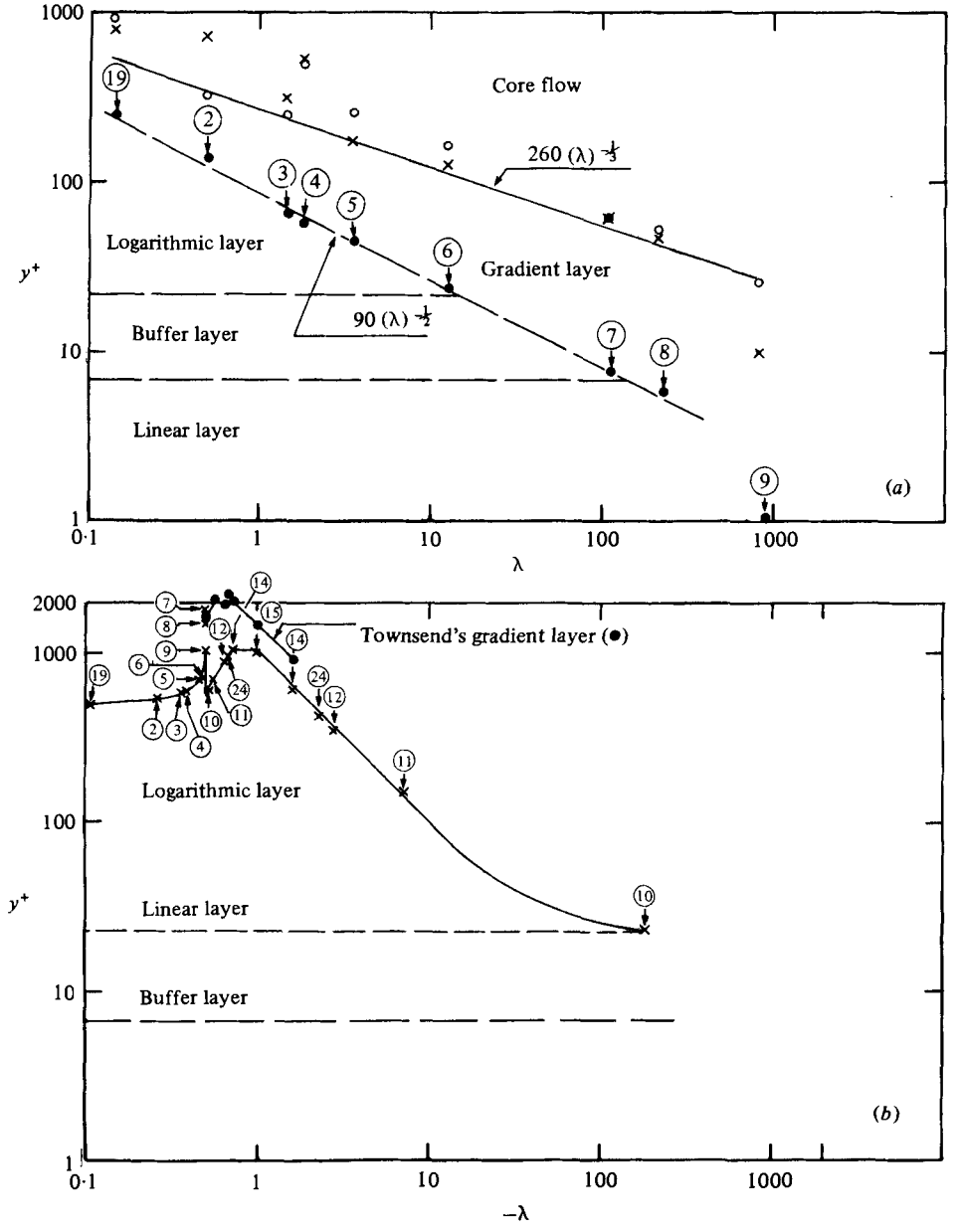

FIGURE 11. Boundaries between regions distinguished within the flows: points × are derived from figures 4 and 5; points ○ are derived from figures 7 and 9. (*a*) Positive stress gradient. (*b*) Negative stress gradient.

flows (from figures 5, 7 and 9). In figure 11(*a*) these boundaries are defined, for $0{\cdot}1 < \lambda < 300$, by the empirical results

$$y_+ = 90\lambda^{-\frac{1}{2}}, \tag{6.1}$$

$$y_+ = 260\lambda^{-\frac{1}{3}}. \tag{6.2}$$

The latter provides a lower bound to the extent of the half-power regions, but even so the gradient layer is typically five times thicker than the constant-stress region. In

some cases the validity of the half-power representation of the velocity profile exceeds the limit (6.2) by a factor of two.

Even for small values of λ, for which an improved representation of the velocity distribution might be expected, Townsend's characterization of the flow (figure 7) does not systematically extend further from the wall than does the simpler form of Kader & Yaglom (figure 5).

In figure 11 (*a*) we note an apparent change in the character of the transition between constant-stress and gradient layers at very large values of λ (> 400, say). A change in the nature of the near-wall flow is also evident in the profile for case 9 shown in figure 4(*b*). For the points marked 6, 7, 8 and 9 in figure 11(*a*) we find $u_*^3/\alpha\nu = 11$, 1·2, 0·35 and 0·03, respectively. Thus it appears that the criterion defining conditions in which the nature of the wall layer changes profoundly is $u_*^3/\alpha\nu < 0{\cdot}3$, say.

Reference to figure 4(*b*) reveals that even for case 10 the standard logarithmic layer is closely, though briefly, approached near the low-stress wall. For this case

$$u_*^3/|\alpha|\,\nu = 0{\cdot}38.$$

Thus it appears that a significant change in the near-wall flow occurs only when $u_*^3/|\alpha|\,\nu < 0{\cdot}3$ for $\alpha < 0$ as well.

We turn now to figure 11 (*b*), which describes wall layers across which the shear stress falls as the wall is left behind. The range of applicability of the logarithmic formula varies rapidly near $-\lambda = 0{\cdot}5$ and is greatest for Poiseuille flow. The gradient layer is not as extensive (where it exists at all), but in some cases it still exceeds the logarithmic layer in thickness. Finally, for large (negative) stress gradients the extent of the constant-stress layer again falls off with increasing stress gradient.

In figure 12 the boundaries between the several regions are shown as functions of y/h, and the positions of maximum velocity (line M) and of zero shear stress (line Z) are superposed. In the following discussion we shall apply the term 'wall layer' to all those parts of the flow that are effectively described by similarity laws incorporating the distance y measured from the adjacent wall. Thus the wall layer comprises viscous, logarithmic and possibly gradient layers. The part of the flow that does not satisfy this criterion is referred to as the 'core'.

For the Couette-type flows we see that the wall layer on the high-stress side occupies perhaps 35% of the channel, extending to 50% or more as the stress falls. The whole of this layer is described by the logarithmic formula of equation (2.11). The wall layer on the low-stress side is at least as thick, but (save for $\gamma \simeq 1$) is composed of a sizeable gradient layer as well as a logarithmic layer. Indeed, for $\gamma \simeq 0$ the viscous layer extends to meet the gradient layer, or at least the region much influenced by the stress gradient. The limit G_2 is the 'conservative' one of figure 11(*a*) and equation (6.2); when it is adopted there remains a substantial core region between the two wall layers. However, many of the individual gradient-layer limits of figure 11(*a*) lie beyond the limit L_1. Hence it is possible to describe the whole of a Couette-type flow using wall-layer formulae, meeting at L_1, say.

For the Poiseuille-type flows the wall layer on the high-stress side extends over at least 50% of the channel, about half of it being adequately described by the gradient-layer model. The extent of the wall layer on the low-stress side is limited by the line M defining the maximum velocities, and the gradient layer is further limited by the line Z defining the zero stress point. Nevertheless, the wall layer occupies from 50%

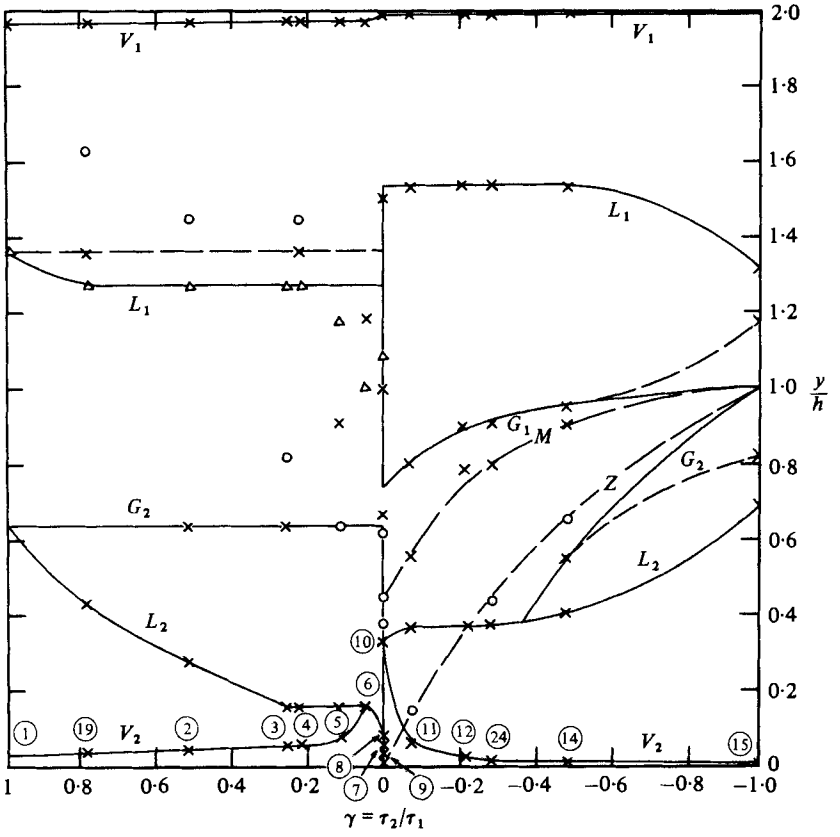

FIGURE 12. Boundaries between regions: V_1, V_2, limits of viscous layers ($y_+ = 22$); L_1, L_2, limits of logarithmic layers (as figure 11); G_1, G_2, limits of gradient or half-power layers (as figure 11). The lines M and Z denote, respectively, points of maximum velocity and zero shear stress (as figure 3). The co-ordinate y is measured from the low-stress wall.

($\gamma \simeq -1$) to 20% ($\gamma \simeq 0$) of the channel. In the latter limit the viscous layer thickens to occupy nearly 20% of the channel.

From figure 12 we see that there are two quite different circumstances in which it is impossible to identify a gradient layer.

(*a*) On the high-stress wall of Couette-type flows ($\gamma > 0$, $-\lambda < 0{\cdot}5$); here there is a deep logarithmic layer and the stress gradient is not sufficiently large to dominate the flow beyond the logarithmic region.

(*b*) On the low-stress wall of some Poiseuille-type flows ($\gamma < 0$, $-\lambda < 2{\cdot}5$); here the influence of the core flow penetrates so close to the wall that the wall layer terminates with the logarithmic region.

Finally, we consider the circumstances in which the viscous region thickens rapidly near $\gamma = 0$. It is plausible to relate this marked extension of the influence of viscosity to the phenomenon of 'relaminarization' often observed in boundary layers subjected to favourable pressure gradients ($\alpha < 0$) for $u_*^3/|\alpha|\nu < 50$. For an adverse pressure gradient ($\alpha > 0$) Kader & Yaglom have argued that this criterion will indicate the onset of intermittent separation of a developing boundary layer. While a developed

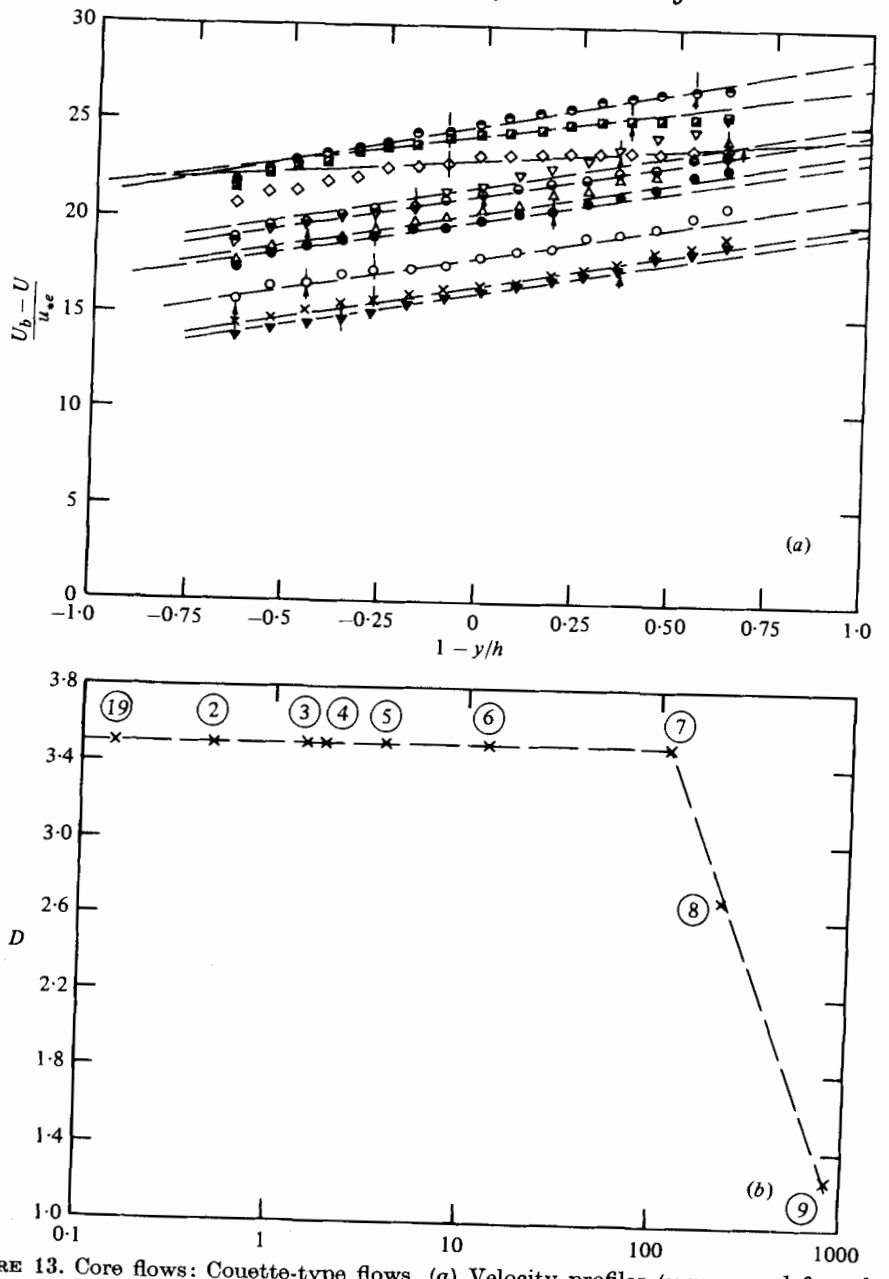

FIGURE 13. Core flows: Couette-type flows. (*a*) Velocity profiles (y measured from low-stress wall) scaled using the friction velocity of equation (6.3). Wall-layer limits (figures 11 and 12) are indicated. See figure 2 for the symbols. (*b*) Slopes of the nearly linear core regions.

channel flow will not experience separation, it is reasonable to suppose that the nature of the near-wall flow will be profoundly influenced if the parameter $u_*^3/\alpha\nu$ is sufficiently small.

Considering cases 5 and 11, which lie just outside the region of rapid extension of the viscous region, we find that

$$u_*^3/\alpha\nu = 75, \; -57.$$

It appears then that the criterion $u_*^3/|\alpha|\nu < 50$ defines conditions in which the viscous layer occupies a significant fraction of the wall layer. On the other hand, we noted earlier that the structure of the wall layer may be substantially unaltered until a much lower value of the parameter $u_*^3/|\alpha|\nu$ (0·3, say) is reached.

6.2. *Core region: Couette-type flows*

The velocities plotted in figure 13 have been scaled using the 'effective' friction velocity

$$u_{*e} = (u_{*1}^2 + u_{*2}^2)^{\frac{1}{2}} = [(|\tau_1| + |\tau_2|)/\rho]^{\frac{1}{2}}, \tag{6.3}$$

which is conceived to represent the turbulent activity in the core region, contributed to by the wall layers on either side. With this scaling the slopes of the core regions of most of the Couette-type flows are virtually the same, only the two most asymmetrical profiles departing from this pattern.

The widely applicable core-region law is seen from figure 13(*b*) to be

$$D = \frac{h}{u_{*e}} \frac{dU}{dy} = 3{\cdot}5. \tag{6.4}$$

The value quoted by Reynolds (1974) for this slope parameter is 2·6, with account taken of the way in which the friction velocity has been defined here (equation (6.3)). The higher value obtained from the present analysis may be attributable to the strict way in which we have defined the core region, omitting points that might in a more superficial analysis have been assigned to the core rather than to the wall layers.

The velocity increment across the linear core region is a rather small fraction of the wall-to-wall velocity change, $\Delta U/u_* < 2{\cdot}5$ compared with $U_b/u_* \sim 30$.

6.3. *Core region: Poiseuille-type flows*

Figure 14(*a*) gives the velocity-defect variations, scaled using the friction velocity of equation (6.3), as functions of distance measured from the point of maximum velocity. The channel depth $2h$ has been adopted as the scale of length; this can be interpreted as the sum of the distances to the two walls from the point of maximum velocity, $y_{m1} + y_{m2}$. It was pointed out in connection with equation (2.16) that for Poiseuille flow itself the velocity defect varies as $(\Delta y/h)^n$ with $n = 1{\cdot}9$; this index proves to give the best approximation to the velocity variations within the more general class of flows considered here.

The scaling adopted in figure 14(*a*) does gather most of the velocity profiles close to a single line

$$\Delta U/u_{*e} = 11{\cdot}5(\Delta y/2h)^{1{\cdot}9}. \tag{6.5}$$

However, the variations on the high-stress side of the two profiles for which $\gamma \simeq 0$ are not well represented. Figure 14(*b*) presents the velocities on the high-stress sides of the flows using velocity and length scales more appropriate to that part of the flow, namely u_{*1} and y_{m1}. All of the profiles are adequately described by the single law

$$\Delta U/u_{*1} = 4{\cdot}4(\Delta y/y_{m1})^{1{\cdot}9}. \tag{6.6}$$

If a like procedure is adopted for the low-stress side of the flows, a different formula is obtained, and the scatter is much greater than that of figure 14(*a*).

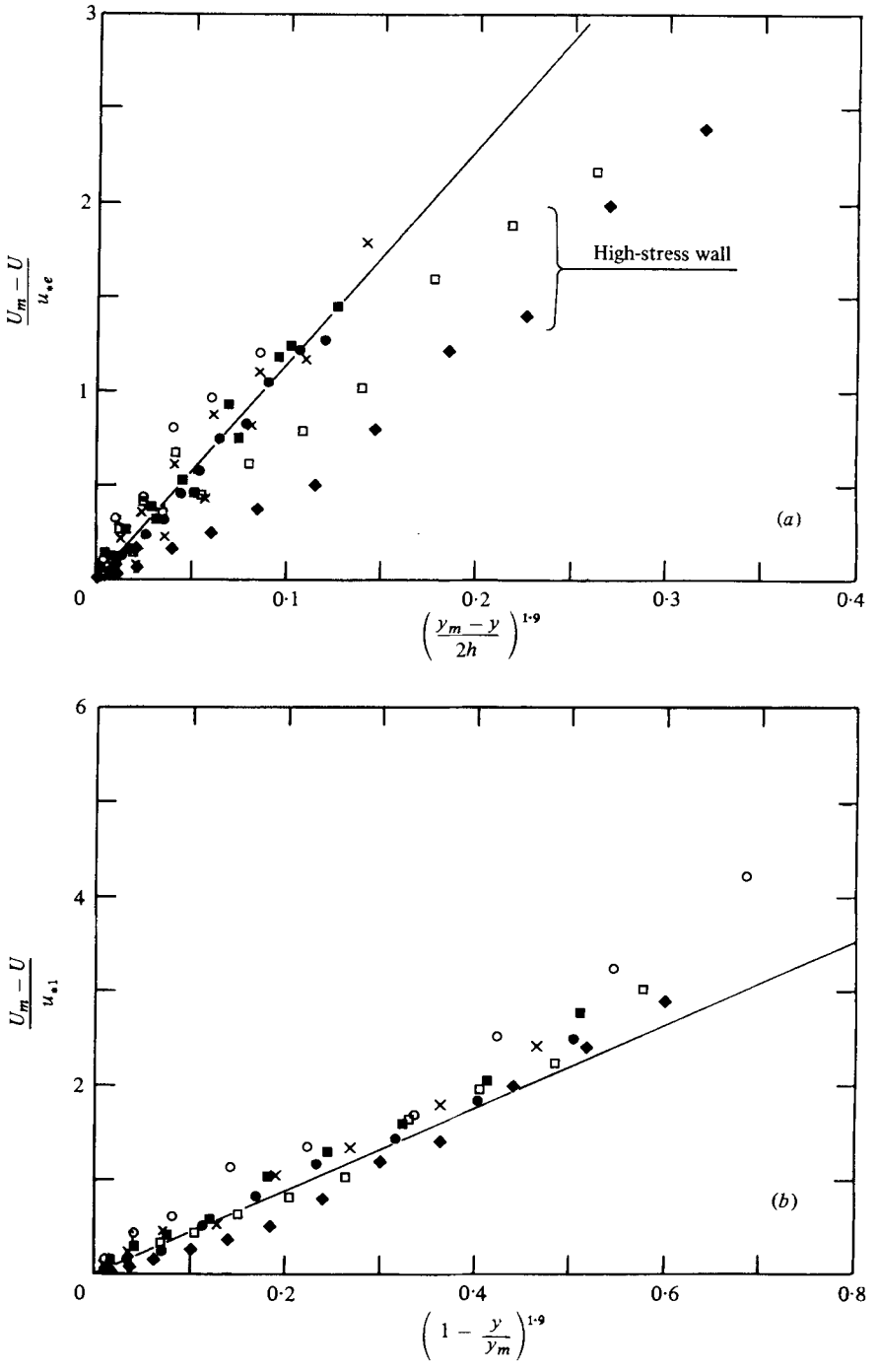

FIGURE 14. Core flows: Poiseuille-type flows. (*a*) Velocity defect scaled using the friction velocity of equation (6.3). (*b*) Velocity defects on the high-stress side scaled using friction velocity and length scale for that part of the flow. ◆, 10; □, 11; ■, 12; ×, 14; ○, 15; ×; ●, 24.

Although the empirical formulae (6.5), (6.6) specify the velocity defects with good accuracy for $\Delta y/h$ or $\Delta y/y_{m1} < 0{\cdot}6$, the outer limits to the wall layer (see figure 12) indicate that the core formulae need be used only over the range $\Delta y/h < 0{\cdot}4$ on the low-stress side and $\Delta y/h < 0{\cdot}3$ on the high-stress side. That is to say, there is a substantial region in which the core and wall-layer laws overlap. Moreover, in the region between the wall layers, we have $\Delta U/u_* < 0{\cdot}5$, showing that a very precise prescription of the core velocity is not required for many purposes.

The constant in the empirical law (6.5) is somewhat lower than that appropriate to Poiseuille flow alone. This is evident in figure 14 and is also suggested by the empirical value $R_f = 13$ (see equation (2.15)) quoted by Reynolds (1974), which indicates a constant around 18 in a law of the form (6.5).

7. Conclusions

A number of conclusions concerning specific aspects of these flows have been noted in the body of the paper; here we attempt to identify matters of more general application.

Townsend's analysis, leading to equation (2.11), provides an adequate description of the velocity variation through large parts of these flows. When generalized, his results are of wider application than Kader & Yaglom's piece-wise representation of the wall layer; but, when the two formulations are applicable ($\alpha > 0$), there is little to choose between them. For both it is necessary that the two constants characterizing the gradient layer are varied in an appropriate manner with some parameter specifying the stress gradient, as Kader & Yaglom pointed out would be the case.

For positive stress gradients the influence of the gradient on the wall layers of these channel flows is substantially that found by Kader & Yaglom for developing boundary layers. This suggests that the empirical wall-layer models derived here could be applied profitably in the analysis of boundary layers.

Although earlier discussions of the gradient layer have concentrated on boundary layers near separation, where the stress gradient is positive, Townsend's results have been found to apply equally to flows with negative stress gradients. Indeed, the empirical laws are of simpler form in those cases of negative stress gradient for which gradient layers are found to exist.

The influence of the pressure gradient (or, as we view it here, the stress gradient) on the viscous layer appears to be more complex than has been realized. While the viscous layer starts to thicken rapidly when the accepted criterion for wall-layer relaminarization is reached, there is some evidence that the structure of the wall layer remains substantially unaltered until a much more stringent condition is satisfied.

Finally, the most appropriate velocity scale for the core regions of most of these flows appears to be the friction velocity based on the sum of the absolute values of the two wall stresses.

The apparatus used in these experiments was in large measure designed and developed by Dr M. Farrashkhalvat and Mr M. Kalirai, formerly students of Brunel University. The first author has also to acknowledge with thanks the financial assistance of the Egyptian Education Bureau during this investigation.

Appendix. Limiting theory for $\tau = \rho\alpha y$

The prediction of K_2 in the half-power law based on matching with a constant-stress viscous layer is unrealistic when $\Gamma < 0{\cdot}9$. For $\tau_w \simeq 0$ the shear stress distribution can be expressed as

$$\tau = \rho\alpha y.$$

Hence in the viscosity-dominated region

$$\mu \frac{dU}{dy} = \rho\alpha y. \tag{A 1}$$

The integral of equation (A 1) may be written as

$$U = \frac{1}{2}\frac{\alpha}{\nu} y^2. \tag{A 2}$$

Matching the gradient layer result

$$\frac{U}{u_*} = K_1 \left(\frac{\alpha y}{u_*^2}\right)^{\frac{1}{2}} + K_2$$

with equation (A 2), we obtain

$$K_2 = \frac{1}{2}\left(\frac{\alpha\nu}{u_*^3}\right)(y^+)^2 + K_1 \left(\frac{\alpha\nu}{u_*^3} y^+\right)^{\frac{1}{2}}. \tag{A 3}$$

Differentiation of equation (A 3) gives

$$y^+ = (\tfrac{1}{2}K_1)^{\frac{2}{3}} \left(\frac{\alpha\nu}{u_*^3}\right)^{-\frac{1}{3}} \tag{A 4}$$

and substitution into equation (A 3) gives

$$K_2 = -\frac{3}{4 \times 2^{\frac{1}{3}}} (\Gamma')^{-\frac{2}{3}} \left(\frac{u_*^3}{\alpha\nu}\right)^{\frac{1}{3}},$$

where

$$\Gamma' = \frac{u_*^3}{\alpha\nu}\frac{1}{K_1^2}.$$

Note that the constant K_2 is no longer a function of the single parameter Γ, but has a separate dependence on $u_*^3/\alpha\nu$. The prediction of K_2 for case 9 using this theory (see figure 6*b*) is in good agreement with the measured value.

REFERENCES

Comte-Bellot, G. 1965 Ecoulement turbulent entre deux parois parallèles. *Publications Scientifiques et Techniques du Ministère de l'air* no. 419.

Constantinescu, V. N. 1959 On turbulent lubrication. *Proc. Inst. Mech. Eng.* **173**, 881–900.

Hanjalić, K. & Launder, B. E. 1972 Fully developed asymmetric flow in a plane channel. *J. Fluid Mech.* **51**, 301–335.

Hinze, J. O. 1975 *Turbulence*, 2nd edn. McGraw-Hill.

Huey, L. J. & Williamson, J. W. 1974 Plane-turbulent Couette flow with zero-net flow. *Trans. A.S.M.E.* E, *J. Appl. Mech.* **41**, 885–890.

Hussain, A. K. M. F. & Reynolds, W. C. 1975 Measurements in fully developed turbulent channel flow. *Trans. A.S.M.E.* I, *J. Fluids Engng* **97**, 568–578.

KADER, B. A. & YAGLOM, A. M. 1978 Similarity treatment of moving-equilibrium turbulent boundary layers in adverse pressure gradients. *J. Fluid Mech.* **89**, 305–342.

LAUFER, J. 1951 Investigation of turbulent flow in a two-dimensional channel. *N.A.C.A. Rep.* 1053.

REYNOLDS, A. J. 1963 Analysis of turbulent bearing films. *J. Mech. Engng Sci.* **5**, 258–272.

REYNOLDS, A. J. 1965 Wall layers with non-uniform shear stress. *J. Fluid Mech.* **22**, 443–448.

REYNOLDS, A. J. 1974 *Turbulent Flows in Engineering.* Wiley.

ROBERTSON, J. M. & JOHNSON, H. F. 1970 Turbulence structure in plane Couette flow. *Proc. A.S.C.E., J. Engng Mech.* **96**, 1171–1182.

SAIBEL, E. A. & MACKEN, N. A. 1974 Nonlaminar behaviour in bearings. A critical review of the literature. *Trans. A.S.M.E.* F, *J. Lub. Tech.* **96**, 174–181.

SZERI, A. A., YATES, C. C. & HAI, S. M. 1976 Flow development in parallel plate channel. *Trans. A.S.M.E.* F, *J. Lub. Tech.* **98**, 145–156.

TOWNSEND, A. A. 1961 Equilibrium layers and wall turbulence. *J. Fluid Mech.* **11**, 97–120.